High-Resolution Photon Counting Using a Lens-Coupled EMCCD Gamma Camera

Todd C. Soesbe, *Member, IEEE*, Matthew A. Lewis, *Member, IEEE*, Nikolai V. Slavine, Edmond Richer, Frederick J. Bonte, and Peter P. Antich, *Senior Member, IEEE*

***Abstract*—A lens-coupled electron multiplying charge-coupled device (EMCCD)-based gamma camera capable of performing photon counting for both ^{99m}Tc and ^{125}I sources has been constructed. This system differs from previous EMCCD-based gamma cameras by using lens-coupling rather than fiber-optic coupling to transfer the light from the scintillating crystal to the EMCCD. The gamma camera described herein uses a micro-columnar CsI(Tl) crystal, two $f/0.95$ lenses, and a commercial camera containing the e2v CCD97 EMCCD that was cooled to $-70\,^{\circ}$C. Acquisition of the video-rate frames from the CCD97 was performed using LabVIEW software. Real-time photon counting analysis of the individual scintillation flashes within the CCD97 frames was performed by using the LabVIEW IMAQ software module. An intrinsic resolution of 56 μm FWHM was measured by using a 25 μm slit collimator and ^{125}I source. A single 0.5 mm diameter pinhole collimator was used for SPECT reconstruction of a mouse thyroid gland containing 100 μCi (3.7 MBq) of ^{125}I uptake. We found that although the photopeak for ^{99m}Tc (140 keV) could be resolved, the photopeak for ^{125}I ($\approx$ 27 keV) could not be fully resolved due to the low optical transfer efficiency of dual lens coupling ($<$ 5%). Nonetheless, energy windowing for ^{125}I sources was used to eliminate most of the background events, proving that high-resolution photon counting for low-energy sources can be achieved by using simple lens-coupling.**

***Index Terms*—EMCCD, gamma camera, high-resolution, high-sensitivity, pinhole collimator, preclinical, small animal, SPECT.**

I. Introduction

In A PREVIOUS publication, we described a high-resolution gamma camera that used a lens-coupled electron multiplying CCD (EMCCD) as the photodetector [1]. This previous system used a 3-mm-thick monolithic CsI(Tl) crystal, two $f/0.95$ lenses, and a homebuilt camera that contained the inexpensive (U.S.$500) Texas Instruments Impactron™ TC253 front-illuminated EMCCD (TC253SPD-B0) [2]–[5]. The TC253 EMCCD system displayed a high intrinsic resolution (110 μm FWHM) and pinhole SPECT reconstruction capabilities for ^{99m}Tc sources. The TC253 results were obtained by using light integration images with exposure times of several minutes. We found that the inherent spurious charge generation (i.e., non-photon-related clock induced charge) [6] at high gain (3 to 4 electrons/pixel) [7] and low quantum efficiency (35% at 560 nm) of the TC253 made it incapable of photon counting for ^{99m}Tc and ^{125}I sources using lens coupling.

EMCCD photon counting is a method in which both the position and energy of the individual scintillation flashes within the CsI(Tl) crystal are measured in real time and are saved as list-mode data [8]–[12]. This is achieved by using video-rate image acquisition with exposure times that are tens of milliseconds long. The photon counting method is analogous to those used by PMT-based gamma cameras [13]. EMCCD photon counting gives a higher intrinsic resolution compared to long-exposure light integration images, plus it allows for energy windowing (not possible with light integration) to reduce the number of scattered and background events [8], [10].

In order to perform photon counting with a lens-coupled EMCCD, the previous TC253 system was modified in two main ways. First, the monolithic CsI(Tl) crystal was replaced with micro-columnar CsI(Tl) crystal. Second, the homebuilt TC253-based camera was replaced with a high-quality commercial camera that contained the e2v Technologies CCD97 EMCCD [14]. We show that although the lens configuration did not change, the crystal and EMCCD changes were enough to improve the signal-to-noise ratio (SNR) to a point where photon counting could be achieved. Details of the hardware changes, photon counting software, and initial results follow.

II. Materials and Methods

A. Hardware

A schematic of the new CCD97 system is shown in Fig. 1. Details of the scintillating crystal, lenses, and EMCCD camera will be described.

1) Scintillating Crystal: For the scintillating crystal, we used a Hamamatsu J6675-01 FOS (fiber optic plate with CsI(Tl) scintillator). This FOS model has a 150 μm-thick micro-columnar CsI(Tl) crystal that is optically coupled to a 3-mm-thick fiber optic plate (FOP, 6 μm fiber diameter). While this crystal thickness will stop $\approx$ 85% of incident ^{125}I radiation ($\approx$ 27 keV), it will stop only $\approx$ 5% of ^{99m}Tc radiation (140 keV). In order to stop a higher percentage of ^{99m}Tc radiation and improve overall detector sensitivity, a thicker crystal must be used. The benefits

Manuscript received July 07, 2009; revised January 12, 2010; accepted February 22, 2010. Date of current version June 16, 2010. This work was supported in part by the DOD BCRP Idea Award Grant W81-XWH-0410551 and in part by the NIH and National Cancer Institute U24 CA126608-SAIRP.

T. C. Soesbe was with the Radiological Sciences Graduate Program, The University of Texas Southwestern Medical Center at Dallas, Dallas, TX 75390-9058 USA. He is now with the Advanced Imaging Research Center at The University of Texas Southwestern Medical Center at Dallas, Dallas, TX 75390-8568 USA (e-mail: todd.soesbe@utsouthwestern.edu).

M. A. Lewis, N. V. Slavine, and P. P. Antich are with the Division of Advanced Radiological Sciences, The University of Texas Southwestern Medical Center at Dallas, Dallas, TX 75390-9058 USA.

E. Richer is with the Department of Mechanical Engineering at Southern Methodist University, Dallas, TX, 75275-0337 USA.

F. J. Bonte is with the Nuclear Medicine Center, The University of Texas Southwestern Medical Center at Dallas, Dallas, TX 75390-9061 USA.

Color versions of one or more of the figures in this paper are available online at http://ieeexplore.ieee.org.

Digital Object Identifier 10.1109/TNS.2010.2044421

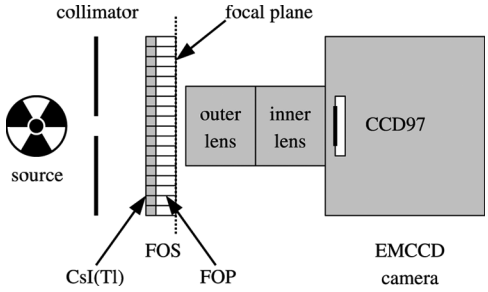

Fig. 1. Schematic of the CCD97 gamma camera setup. Two lenses are used to improve the optical transfer of the scintillation light from the FOS to the EMCCD. The lens focal plane (dotted line) is placed at the exit surface of the FOS.

and consequences of using a thicker crystal are discussed in Section IV.

We found that micro-columnar crystal was better suited for lens-coupled photon counting than monolithic crystal. When using a monolithic CsI(Tl) crystal, the shallow focal plane of the two lenses (< 1 mm thick) is scanned through the crystal until the maximum number of events are in focus. This corresponds to the first few millimeters of gamma ray penetration into the crystal, where the absorption curve is the steepest. Scintillation events occurring outside of the lens focal plane are either too blurred or faint to be counted, which reduces the overall sensitivity of the detector. For micro-columnar CsI(Tl) crystal, the focal plane was simply set at the exit surface of the FOS. Due to the columnar nature of the crystal and fiber optic plate, each scintillation event appears as a small bright spot on the exit surface. Although the spot size and intensity are somewhat dependant on the depth on interaction within the crystal [9], [12], the dependence is much less than that of monolithic crystal. Having all of the scintillation events in focus greatly improves the sensitivity and energy resolution capabilities of lens-coupled photon counting.

2) Lenses: Two 1-inch format lenses (Schneider Xenon 0.95/25) were fastened front-to-front using a brass coupler. The inner lens was then fastened to the C-mount of the EMCCD camera. The f-stop for each lens was set to 0.95, with the outer lens focus set to infinity. The FOS was held at a fixed distance (≈ 1 cm) from the outer lens using a brass coupler that fastened to the outer lens C-mount. The focus of the inner lens was then adjusted so that the focal plane was at the exit surface of the FOS. This macro photography configuration improves the optical transfer efficiency at a cost of reducing the field of view at the crystal surface [1], [15]. The maximum crystal area imaged by the dual lens configuration measured $9.5\text{ mm} \times 9.5\text{ mm}$, while the active area of the CCD97 EMCCD is $8.2\text{ mm} \times 8.2\text{ mm}$. This gives an object to image ratio of $\approx 1:1$ for the gamma camera. Methods for imaging field of views (FOV) that are larger than the CCD area are discussed in Section IV.

3) EMCCD Camera: For the EMCCD camera, we used the PhotonMAX 512B by Princeton Instruments [16]. The PhotonMAX 512B is a high-performance camera designed for ultra low-light level imaging and uses the CCD97 EMCCD by e2v Technologies [14], [17], [18]. The CCD97 has 16 μm square pixels (with 100% fill factor) in a 512×512 array, creating an 8.2 mm^2 image area. The back-illuminated CCD97 has a high quantum efficiency (95% at 560 nm) and a low spurious charge generation at high gain (< 0.01 electron/pixel) [1]. The PotonMAX 512B can also cool the CCD97 down to $-70\,^{\circ}\text{C}$ at which point the dark current generation is only 0.044 electrons/pixel per second. The electron gain achieved in the multiplication register of the CCD97 (up to 1000x) effectively eliminates the charge-to-voltage read noise of the output amplifier [19], [20]. These combined characteristics give the PhotonMAX 512B single electron sensitivity. This improved sensitivity gives an EMCCD better SNR for low light level imaging when compared to a conventional CCD [1]. The PhotonMAX 512B camera was operated at maximum gain (1000x), 16-bit video rate readout (5 MHz), and at $-70\,^{\circ}\text{C}$ for all experiments.

B. Software

The real-time acquisition and digital analysis of the individual EMCCD frames was performed by using LabVIEW software (version 8.0) from National Instruments. The frames were first read from the PhotonMAX 512B using the Scientific Imaging ToolKit (SITK version 1.3.6) LabVIEW interface from R Cubed Software. Photon counting analysis was then performed by using the IMAQ Vision software package from LabVIEW. The photon counting algorithm used will be described.

1) Subtract Background: A background image (without any source) was first collected by taking the average of several thousand frames for a given exposure time (e.g., 33 ms). The background image was then saved and subtracted from each EMCCD frame during the data acquisition. A sample background subtracted frame (256×256 pixels shown) and surface plot for two scintillation events (50×50 pixels) are shown in Fig. 2(a) and (b), respectively.

2) Filter Image: The background subtracted frame was then smoothed by using a Gaussian filter to help reduce the high frequency noise. We used a 3×3 kernel with row elements [0 1 0; 1 2 1; 0 1 0]. Fig. 2(c) shows the filtered image while Fig. 2(d) shows the corresponding surface plot. It can be seen that the two scintillation events from Fig. 2(b) have been further resolved at a cost of slightly reducing the dynamic range.

3) Threshold Image: An upper and lower threshold was then placed on the filtered image. The lower threshold was chosen so that the primary gamma-ray and secondary K x-ray interactions [10] were well separated with minimal background events. The upper threshold was set well above the maximum pixel output from the scintillation events. A sample threshold mask is shown in Fig. 2(e) where each scintillation flash appears as a separate particle.

4) Analyze Particles: The particles defined by the threshold mask were then counted and analyzed. A sample of the list-mode data for 10 particles is shown in Fig. 2(f). The mean centroid x and y values of each particle (XM and YM) were taken as the position. The particle energy was then calculated by measuring either the maximum pixel value (MAX), integrated pixel value (IntDen), or area of each particle (Area). Previous applications of photon counting with EMCCDs have used either the

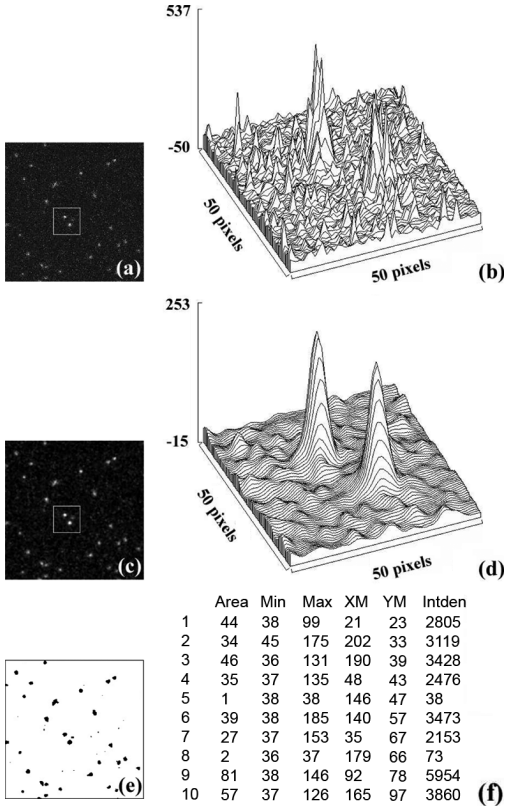

	Area	Min	Max	XM	YM	Intden
1	44	38	99	21	23	2805
2	34	45	175	202	33	3119
3	46	36	131	190	39	3428
4	35	37	135	48	43	2476
5	1	38	38	146	47	38
6	39	38	185	140	57	3473
7	27	37	153	35	67	2153
8	2	36	37	179	66	73
9	81	38	146	92	78	5954
10	57	37	126	165	97	3860

Fig. 2. (a) The 33 ms background subtracted image (256 × 256 pixels) showing individual scintillation events. (b) A surface plot of the two scintillation events selected in (a). (c) The Gaussian filtered image and (d) corresponding surface plot. (e) The threshold mask and (f) a sample of photon counting list-mode data.

maximum pixel value [9] or integrated pixel value [10], [11], [15] of each scintillation event to measure the energy. For our application, we found that the particle area gave the best energy resolution (see Fig. 4).

III. Results

A. Intrinsic Resolution

The intrinsic resolution of the lens-coupled CCD97 gamma camera system was measured by placing a 25 μm slit Tungsten collimator in direct contact with the FOS. An ^{125}I source was then placed in front of the collimator. The activity viewed by the slit was approximately 50 μCi (1.9 MBq). The line spread function for an 11 min exposure (or 20,000 33 ms frames) was acquired. The resulting image and 1-mm-wide line average profile (taken perpendicular to the slit) are shown in Fig. 3. A Gaussian fit to the line profile gave an FWHM of 56 μm which was taken as the intrinsic resolution. This intrinsic resolution is similar to those obtained from fiber-coupled EMCCD gamma camera systems [8]–[11].

B. Energy Resolution

The energy resolution capability of the system was measured by using ^{99m}Tc and ^{125}I. Energy spectra for the two sources and background (no source) were collected separately. Data for each spectrum were collected until the pedestal channel (0 keV) was approximately 55 000 counts. This was done so that each spectrum would have a similar background. Fig. 4(a) shows the three

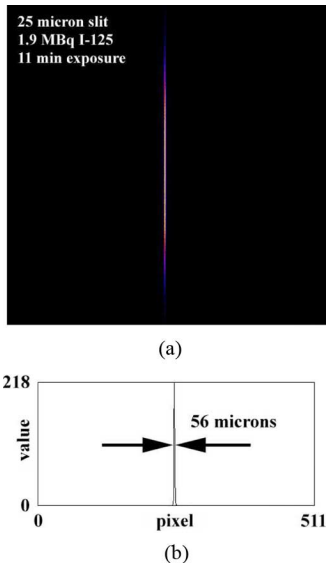

Fig. 3. (a) The 512 × 512 pixel image produced by the 25 μm slit collimator and ^{125}I source. (b) Line profile of (a) showing an FWHM intrinsic resolution of 56 μm.

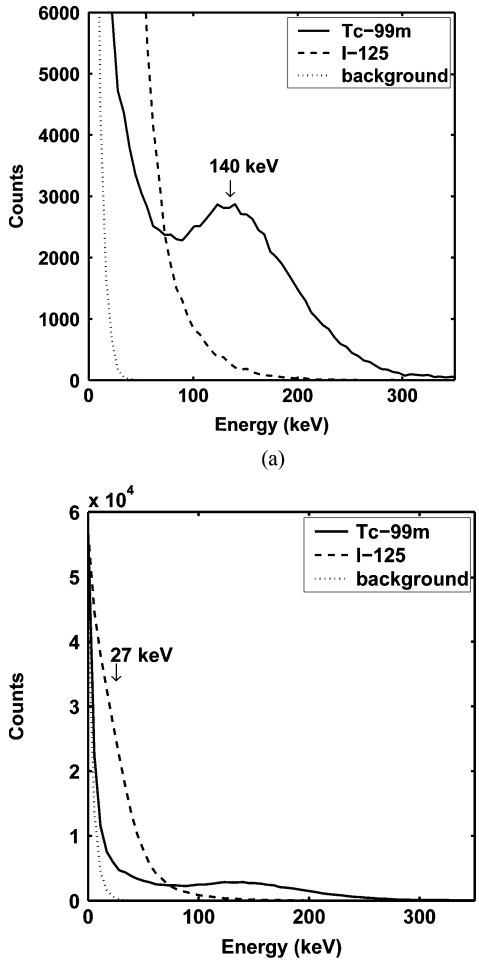

Fig. 4. Energy spectra for ^{99m}Tc, ^{125}I, and the background (no source) scaled for (a) the 140 keV photopeak of ^{99m}Tc, and (b) the ≈ 27 keV photopeak of ^{125}I. The photopeak for ^{125}I is not fully resolved due to the low SNR from lens-coupling.

spectra where the counts have been scaled to view the 140 keV photopeak of ^{99m}Tc. Fig. 4(b) shows the three spectra where

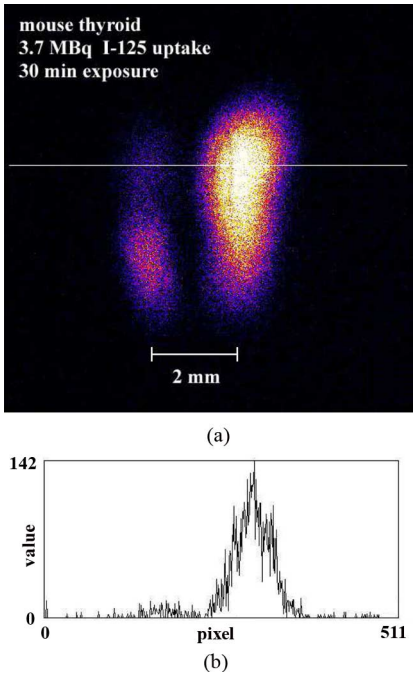

Fig. 5. (a) Single in situ projection image (512 × 512 pixel) of the mouse thyroid produced by the 0.5 mm pinhole. (b) Line profile shown in (a).

the counts have been scaled to view the ≈ 27 keV photopeak of ^{125}I. Although the 140 keV photopeak of ^{99m}Tc could be resolved ($\approx 50\%$ FWHM), due to the low SNR from lens-coupling the $\approx$27 keV photopeak of ^{125}I appears as a shoulder from the pedestal and could not be fully resolved. Nonetheless, energy windowing was used for ^{125}I sources to eliminate most of the background events. These results are similar to those obtained when using a front-illuminated EMCCD with tapered fiber-coupling [8], [21].

C. Mouse Thyroid SPECT

Planar imaging and SPECT reconstruction of ^{125}I uptake within a mouse thyroid gland were performed by using a single pinhole lead collimator. The pinhole diameter was 0.5 mm with an aperture angle of 90°. A healthy mouse was injected with 4 mCi (148 MBq) of ^{125}I, sacrificed after 20 hours, then immediately imaged. A set of projection data (18 projections, 20° step) were taken as the cadaveric mouse was rotated. An exposure time of 3 min per projection was used, giving a total scan time of 1 hour. After imaging, the thyroid gland was excised and measured a total uptake of 100 μCi (3.7 MBq) by using a well counter. An in situ projection image of the ^{125}I uptake within the mouse thyroid is shown in Fig. 5. The asymmetric uptake between the two lobes of the thyroid is due to the natural physiology of the healthy mouse.

SPECT reconstruction was based on the iterative expectation-maximization method (EM) [22]. This method was improved by using a list-mode high-resolution algorithm for system matrix modeling [23], an image de-blurring procedure [24], and realistic resolution modeling [25]. Details of this EMSMD reconstruction method can be found in our previous publication [26].

Fig. 6 shows coronal and axial slices of the EMSMD reconstructed mouse thyroid. Each slice is 0.1 mm thick. The total FOV (8 mm^3) was subdivided into 0.1 mm^3 voxels. Approximately 300 000 events were reconstructed into the voxel array. A Gaussian function (0.2 mm kernel) was used to model the resolution during the 70 iterations. The color scale in Fig. 6 represents the voxel intensity after the final iteration.

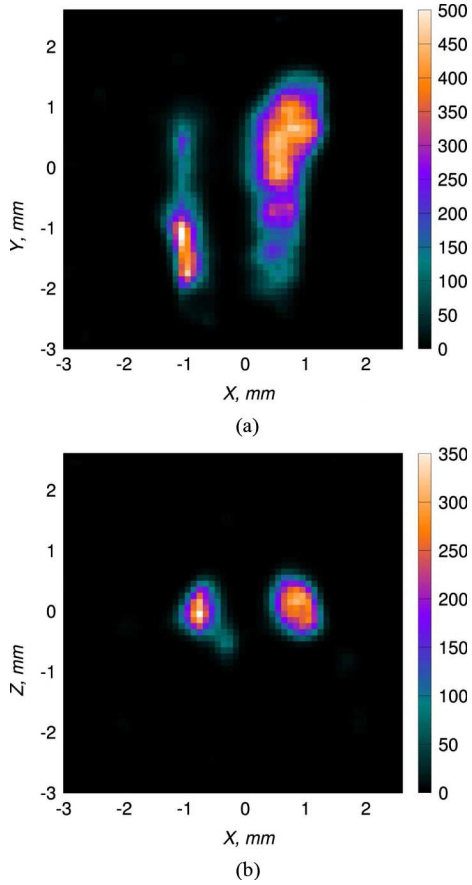

Fig. 6. (a) Coronal slice and (b) axial slice of the EMSMD reconstructed mouse thyroid. Each slice is 0.1 mm thick, with a voxel size of 0.1 mm^3.

IV. Conclusion and Discussion

A. Summary

High-resolution photon counting using a lens-coupled EMCCD gamma camera has been demonstrated. The system used two $f/0.95$ lenses to transfer the scintillation light from a 150 μm-thick micro-columnar CsI(Tl) crystal to an e2v CCD97 EMCCD. The crystal area viewed by the lenses (9.5 mm^2) was approximately the same size as the EMCCD detector area (8.2 mm^2). LabVIEW software was used for both data acquisition from the PhotonMAX 512B EMCCD camera and real-time photon counting analysis to produce list-mode data. An intrinsic resolution of 56 μm FWHM was measured by using a 25 μm slit collimator and ^{125}I source. Energy spectra for ^{99m}Tc and ^{125}I were calculated using the area of the scintillation event. Single pinhole collimation was used for SPECT reconstruction of a mouse thyroid gland containing 100 μCi (3.7 MBq) of ^{125}I uptake.

B. Conclusions

By replacing the monolithic with micro-columnar crystal, and using a high-quality instead of low-quality EMCCD, the SNR of

our lens-coupled gamma camera system has been improved to a point where photon counting can be achieved for both $^{99m}\mathrm{Tc}$ and $^{125}\mathrm{I}$ sources. One advantage of lens-coupling is that there is no direct physical contact with the EMCCD detector surface as with fiber-optic coupling. This greatly reduces the engineering required for cooling the EMCCD and keeping it under vacuum, as the EMCCD can simply be isolated behind an optical window. Although dual-lens coupling offers an improved optical transfer efficiency ($\approx$5%) compared to single lens coupling ($\approx$1%) [1], these values quickly decrease when the viewed crystal area is several times larger than the EMCCD detector area [27]. This currently limits our photon counting application to a crystal area that is approximately the same size as the EMCCD imaging area. Another disadvantage of lens-coupling is that the viewed crystal area has an inhomogeneous response, with the center of the FOV being more sensitive than the edges. This natural vingnetting is an integral property of lenses due to the Cos^4 law of illumination falloff [28]. The FOV homogeneity can be improved, but at a cost of reducing the FOV size at the crystal surface.

Compared to lens-coupling, fiber-optic coupling offers an order of magnitude improvement in optical transfer efficiency, even when the viewed crystal area is several times larger than the EMCCD detector area [27]. The improved optical transfer efficiency and homogeneous FOV response of fiber-optic coupling offer improvements in sensitivity, spatial resolution, and energy resolution that make the engineering requirements associated with using them worthwhile [21].

In order to improve the sensitivity for higher energy sources, such as $^{99m}\mathrm{Tc}$, a thicker micro-columnar CsI(Tl) must be used. With thicker micro-columnar crystal comes an increase in the depth of interaction dependence and cross talk between the crystal columns [15]. These effects increase the variance in spot size and brightness at the crystal surface, which degrade the spatial and energy resolution capabilities of the system. One group has shown that depth of interaction effects from thicker crystals can be corrected for by using a maximum likelihood expectation maximization (MLEM) algorithm to calculate the 3D position and energy estimation of individual scintillation events in real time [12], [29].

C. Discussion

One main challenge when using an EMCCD-based gamma-camera is that even for preclinical imaging, the subject area being imaged (e.g., 30 mm^2) is usually several times larger than the EMCCD detector area (e.g., 10 mm^2). Therefore, some form of image reduction must be used without compromising the resolution and sensitivity performance of the gamma-camera.

Image reduction can be achieved in the gamma ray phase by simply placing a pinhole collimator in front of the EMCCD as shown in Fig. 7, where a is the distance from pinhole to crystal, b is the distance from pinhole to subject, d_e is the effective diameter of the pinhole, and R_i is the intrinsic resolution of the crystal and EMCCD [30]. Although this method minimizes the crystal area (with the crystal and detector area being equivalent), the total resolution is limited by using a b/a ratio that is larger than 1. For example, if $d_e = 0.5$ mm and $R_i = 0.1$ mm, then when $b/a = 3$ (a 30 mm^2 subject area), the total resolution is only 2 mm. The total resolution could be improved by reducing the pinhole diameter, but this would severely reduce the geometric efficiency and, thus, detector sensitivity.

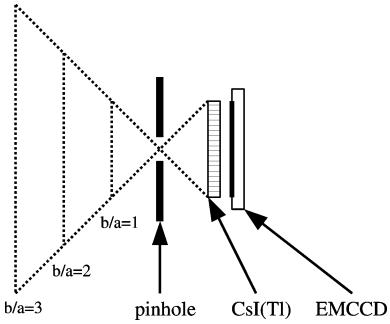

Fig. 7. Image reduction in the gamma ray phase using a pinhole collimator. The total resolution is limited by a $b/a > 1$.

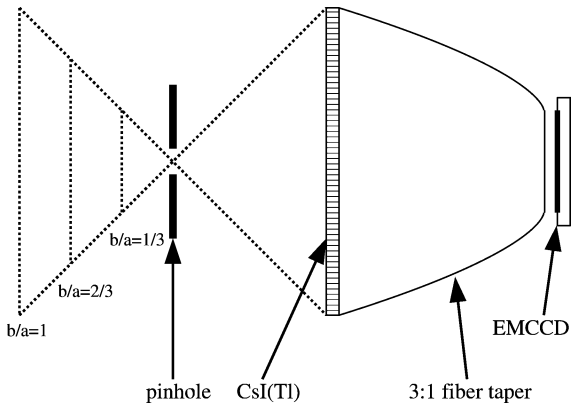

Fig. 8. Image reduction in the optical photon phase by using a fiber-optic taper. The lower b/a ratios improve the total resolution.

Improved total resolution can be achieved by performing image reduction in the optical photon phase as shown in Fig. 8. By using a fiber-optic taper, the effective detector area of the EMCCD is increased, with a 3:1 fiber taper being shown in Fig. 8. With the crystal area now matching the enlarged EMCCD detector area (30 mm^2), a reduced b/a ratio is achieved for similar subject areas compared to Fig. 7. For example, using the previous values for d_e and R_i, a subject area of 30 mm^2 ($b/a = 1$) now gives a total resolution of 1 mm. This method of image reduction is currently used by several groups [8]–[10], [21], [31].

Image reduction can also be achieved in the electron phase by using an image intensifier as shown in Fig. 9. The optical photons from the scintillating crystal are first converted to electrons by the photocathode of the image intensifier. The image intensifier (Generation 1 shown) then uses electrostatic potentials to project a reduced image onto the output phosphor, which converts the electrons back into optical photons. The optical photons from the output phosphor are then transferred to the EMCCD using a fiber-optic bundle. Although the total detector volume for the image intensifier system is much larger compared to an EMCCD alone, it allows for high-resolution photon counting over large subject areas ($\approx$ 50 mm^2) [11], [32].

Another advantage of using an image intensifier is that by replacing the Generation 1 intensifier in Fig. 9 with a Generation 2 or 3 intensifier (S-25 or GaAsP photocathode, respectively, with micro-channel plate), an electron gain of 10^4 to 10^7 can be achieved. Having the electron gain occur in the image intensifier

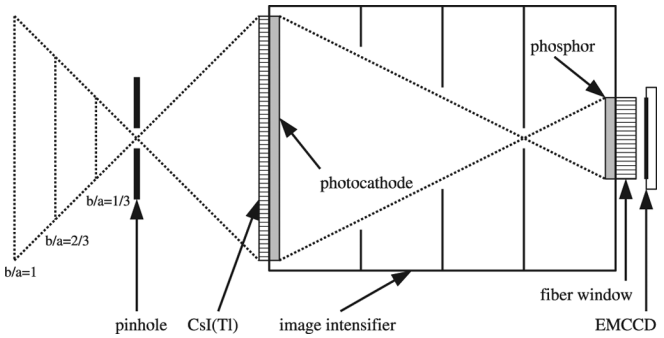

Fig. 9. Image reduction in the electron phase using a Generation 1 image intensifier.

rather than the EMCCD allows the use of a less expensive conventional CCD for image capture and photon counting. Photon counting and SPECT reconstruction using an image intensifier and conventional CCD have been shown by another group [15]. This group used dual-lens coupling to transfer the light from the image intensifier output screen to the CCD detector area. Having the signal gain occur before the lens coupling allowed for an 8:1 subject to image ratio without loss in detector sensitivity or resolution.

Therefore, in order to perform photon counting with an EMCCD/CCD-based gamma camera and image an area larger than the EMCCD/CCD detector area, one could use either 1) an EMCCD with a fiber-optic taper or Generation 1 image intensifier, or 2) a conventional CCD with a lens-coupled Generation 2 or 3 image intensifier.

ACKNOWLEDGMENT

The authors would like to thank Dr. P. Kulkarni, Dr. V. Arora, Dr. A. Constantinescu, M. Lin, B. Smith, and T. Nguyen of the Division of Advanced Radiological Sciences at the University of Texas Southwestern Medical Center at Dallas, and Dr. F. Beekman and J. Heemskerk of the Physics of Molecular Imaging and Nuclear Medicine Group at the University of Utrecht for their technical assistance with this work.

REFERENCES

[1] T. C. Soesbe, M. A. Lewis, E. Richer, N. V. Slavine, and P. P. Antich, "Development and evaluation of an EMCCD gamma camera for preclinical SPECT imaging," *IEEE Trans. Nucl. Sci.*, vol. 54, no. 5, pt. 1, pp. 1516–1524, Oct. 2007.

[2] J. Hynecek, "CCM-a new low-noise charge carrier multiplier suitable for detection of charge in small pixel CCD image sensors," *IEEE Trans. Electron Devices*, vol. 39, no. 8, pp. 1972–1975, Aug. 1992.

[3] J. Hynecek, "Impactron-a new solid state image intensifier," *IEEE Trans. Electron Devices*, vol. 48, no. 10, pp. 2238–2241, Oct. 2001.

[4] J. Hynecek and T. Nishiwaki, "Excess noise and other important characteristics of low light level imaging using charge multiplying CCDs," *IEEE Trans. Electron Devices*, vol. 50, no. 1, pp. 239–245, Jan. 2003.

[5] *Designer's Guide for the TC253SPD/TX253SPD Impactron CCD*. Dallas, TX: Texas Instruments Incorporated, 2003.

[6] J. R. Janesick, *Scientific Charge-Coupled Devices*, 1st ed. Bellingham, WA: SPIE, 2001, pp. 605–654.

[7] P. Jerram, P. Pool, R. Bell, D. Burt, S. Bowring, S. Spencer, M. Hazelwood, I. Moody, N. Catlett, and P. Heyes, "The L3CCD: Low light imaging without the need for an intensifier," in *Proc. SPIE*, 2001, vol. 4306, pp. 178–186.

[8] F. J. Beekman and G. A. de Vree, "Photon-counting versus an integrating CCD-based gamma camera: Important consequences for spatial resolution," *Phys. Med. Biol.*, vol. 50, pp. N109–N119, May 2005.

[9] G. A. de Vree, A. H. Westra, I. Moody, F. van der Have, K. M. Ligtvoet, and F. J. Beekman, "Photon-counting gamma camera based on an electron-multiplying CCD," *IEEE Trans. Nucl. Sci.*, vol. 52, no. 3, pt. 1, pp. 580–588, Jun. 2005.

[10] V. V. Nagarkar, I. Shestakova, V. Gaysinskiy, B. Singh, B. W. Miller, and H. B. Barber, "Fast X-ray/γ-ray imaging using electron multiplying CCD-based detector," *Nucl. Instrum. Meth. Phys. Res. A*, vol. 563, pp. 45–48, Feb. 2006.

[11] L. J. Meng, "An intensified EMCCD camera for low energy gamma ray imaging applications," *IEEE Trans. Nucl. Sci.*, vol. 53, no. 4, pp. 2376–2384, Aug. 2006.

[12] B. W. Miller, B. H. Bradford, H. H. Barrett, I. Shestakova, B. Singh, and V. V. Nagarkar, "Single-photon spatial and energy resolution enhancement of a columnar CsI(TL)/EMCCD gamma-camera using maximum-likelihood estimation," *Proc. SPIE. 6142, 61421T*, 2006.

[13] H. O. Anger, "Scintillation camera," *Rev. Scientif. Instrum.*, vol. 29, no. 1, pp. 27–33, Jan. 1958.

[14] E2V Technologies, 2007. [Online]. Available: www.e2v.com

[15] B. W. Miller, B. H. Bradford, H. H. Barrett, D. W. Wilson, and L. Chen, "A low-cost approach to high-resolution, single-photon imaging using columnar scintillators and image intensifiers," in *Proc. IEEE Nuclear Science Symp. Conf. Rec.*, Oct. 2006, vol. 6, pp. 3540–3545.

[16] P. Instruments, 2007. [Online]. Available: www.piacton.com

[17] The Use of Multiplication Gain in L3Vision™ Electron Multiplying CCD Sensors, Low-Light. Chelmsford, Essex, U.K., e2v Technologies Ltd., Jul. 2003, Tech. Note 2.

[18] Dark signal and clock-induced charge in L3Vision™ CCD sensors. Chelmsford, Essex, U.K., E2v Technologies Ltd., Jul. 2004, Low-Light Tech. Note 4.

[19] On-chip multiplication gain. Tucson, AZ, Roper Scientific, Inc., 2003, Tech. Note 14.

[20] M. S. Robbins and B. J. Hadwen, "The noise performance of electron multiplying charge-coupled devices," *IEEE Trans. Electron Devices*, vol. 50, no. 5, pp. 1227–1232, May 2003.

[21] J. W. T. Heemskerk, A. H. Westra, P. M. Linotte, K. M. Ligtvoet, W. Zbijewski, and F. J. Beekman, "Front-illuminated versus back-illuminated photon-counting CCD-based gamma camera: Important consequences for spatial resolution and energy resolution," *Phys. Med. Biol.*, vol. 52, pp. N149–N162, 2007.

[22] L. A. Shepp and Y. Vardi, "Maximum likelihood reconstruction for emission tomography," *IEEE Trans. Med. Imag.*, vol. MI-1, no. 2, pp. 113–122, Oct. 1982.

[23] A. J. Reader, S. Ally, F. Bakatselos, R. Manavaki, R. J. Walledge, A. P. Jeavons, P. J. Julyan, S. Zhao, D. L. Hastings, and J. Zweit, "One-pass list-mode em algorithm for high resolution 3-d pet image reconstruction into large arrays," *IEEE Trans. Nucl. Sci.*, vol. 49, no. 3, pt. 1, pp. 693–699, Jun. 2002.

[24] P. Antich, R. Parkey, S. Seliounine, N. Slavine, E. Tsyganov, and A. Zinchenko, "Application of expectation maximization algorithms for image resolution improvement in a small animal PET system," *IEEE Trans. Nucl. Sci.*, vol. 52, no. 3, pt. 1, pp. 684–690, Jun. 2005.

[25] E. N. Tsyganov, J. Anderson, G. Arbique, A. Constantinescu, M. Jennewein, P. V. Kulkarni, R. P. Mason, R. W. McColl, O. K. Oz, R. W. Parkey, E. Richer, F. Rosch, S. Y. Seliounine, N. V. Slavine, S. C. Srivastava, P. E. Thorpe, A. I. Zinchenko, and P. P. Antich, "UTSW small animal positron emission imager," *IEEE Trans. Nucl. Sci.*, vol. 53, no. 5, pp. 2591–2600, Oct. 2006.

[26] N. V. Slavine and P. P. Antich, "Practical method for radioactivity distribution analysis in small-animal PET cancer studies," *Appl. Rad. Isotopes*, vol. 66, pp. 1861–1869, 2008.

[27] S. M. Gruner, M. W. Tate, and E. F. Eikenberry, "Charge-coupled device area X-ray detectors," *Rev. Scientif. Instrum.*, vol. 73, pp. 2815–2842, 2002.

[28] W. Yu, "Practical anti-vignetting methods for digital cameras," *IEEE Trans. Consum. Electron.*, vol. 50, no. 4, pp. 975–983, Nov. 2004.

[29] D. Marks, H. Barber, H. Barrett, and J. Eskin, "Maximum-likelihood estimation for semiconductor detector arrays," in *Proc. IEEE Nuclear Science Symp.*, 1997, pp. 551–555.

[30] H. O. Anger, "Radioisotope cameras," in *Instrumentation in Nuclear Medicine*, G. J. Hine, Ed. London, U.K.: Academic Press, 1967, vol. 1, ch. 19, pp. 485–553.

[31] V. V. Nagarkar, I. Shestakova, V. Gaysinskiy, S. V. Tipnis, B. Singh, W. Barber, B. Hasegawa, and G. Entine, "A CCD-based detector for spect," *IEEE Trans. Nucl. Sci.*, vol. 53, no. 1, pt. 1, pp. 54–58, Feb. 2006.

[32] L. J. Meng, N. H. Clinthorne, S. Skinner, R. V. Hay, and M. Gross, "Design and feasibility study of a single photon emission microscope system for small animal I-125 imaging," *IEEE Trans. Nucl. Sci.*, vol. 53, no. 3, pt. 2, pp. 1168–1178, Jun. 2006.